Miniature side-view dual axes confocal endomicroscope for repetitive in vivo imaging

Ahmad Shirazi,[1] Tayebeh Sahraeibelverdi,[2] Miki Lee,[3] Haijun Li,[3] Joonyoung Yu,[2] Sangeeta Jaiswal,[3] Kenn R Oldham,[2] and Thomas D Wang[2,3,4,*]

[1]*Division of Integrative Systems and Design, University of Michigan, Ann Arbor, MI 48109, USA*
[2]*Department of Mechanical Engineering, University of Michigan, Ann Arbor, MI 48109, USA*
[3]*Department of Internal Medicine, Division of Gastroenterology, University of Michigan, Ann Arbor, MI 48109, USA*
[4]*Department of Biomedical Engineering, University of Michigan, Ann Arbor, MI 48109, USA*
[*]*thomaswa@umich.edu*

Abstract: A side-view dual axes confocal endomicroscope is demonstrated that can be inserted repetitively in hollow organs of genetically engineered mice for in vivo real-time imaging in horizontal and vertical planes. Near infrared (NIR) excitation at $\lambda_{ex} = 785$ nm was used. A monolithic 3-axis parametric resonance scan mirror was fabricated using micro-electro-mechanical systems (MEMS) technology to perform post-objective scanning in the distal end of a 4.19 mm diameter instrument. Torsional and serpentine springs were designed to "switch" the mode of imaging between vertical and horizontal planes by tuning the actuation frequency. This system demonstrated real-time in-vivo images in horizontal and vertical planes with 310 µm depth and 1.75 and 7.5 µm lateral and axial resolution. Individual cells and discrete mucosal structures could be identified.

1. Introduction

Confocal laser endomicroscopy is an emerging technology for in vivo imaging whereby microscopes are scaled down in size to millimeter dimensions to image internal organs with sub-cellular resolution [1–4]. The core of an optical fiber acts as a spatial filter to allow only the light that originates from the plane of focus below the tissue surface to be collected [5]. Fluorescence images can be collected in vivo to track the behavior of individual cells in the natural microenvironment. Repetitive imaging can be performed to extend the time course for visualizing important dynamic events and to better understand normal development and the natural history of disease processes. Each animal can be used as its own control to reduce the numbers needed for statistical rigor. The reduced instrument size may be compatible with medical endoscopes to perform "instantaneous" histology. By comparison, conventional intra-vital microscopes are tabletop systems equipped with bulky optics and scan mechanisms [6–8]. Either wide surgical exposure or surgically implanted optical windows are needed [9–11]. These procedures can cause significant trauma, and the application of pressure reduces blood flow, causes hypoxia, and incurs biological artifacts.

The dual axes confocal architecture is a unique approach to perform optical sectioning that uses separate illumination and collection beams [12–15]. This method has been previously reported for use in a variety of medical applications, including gastrointestinal endoscopy [16], dermatopathology [17,18] and neurosurgery [19,20]. In the dual axes architecture, two optical fibers and two low numerical aperture (NA) objectives are oriented at an angle to the main optical axis. The region of overlap between these beams defines the focal volume and significantly reduces the resolution achieved by either objective alone. Light scattered by tissue along the illumination path enters the collection optics at large angles and is not captured [21]. This effect

improves the dynamic range so that images can be collected in vertical and horizontal planes. Vertical cross-sections provide the same view as that used by pathologists to evaluate histology [22]. The low NA objectives create a long working distance (WD) so that the scan mirror can be placed in the post-objective position distal to the primary focusing optics. This location allows for images to be collected with a very large field-of-view (FOV). The optical design can be scalable, so that the instrument diameter and overall size can be markedly reduced without loss of resolution. This configuration has been previously demonstrated in an endomicroscope with 5.5 mm diameter [16,23]. However, this instrument was too large for in vivo use in hollow organs of mice, and the front-view orientation limited access to tissues of interest.

Frame rates >5 Hz have been used to perform real time in-vivo imaging, as reported in the literature. An increase in the imaging speed can be achieved by changing the illumination pattern, such as with line [24–27] and plane [28,29] scanning. Although the frame rate significantly improves, performance in the direction perpendicular to the scan direction is degraded due to the loss of confocality. Also, the need for bulky optics and expensive detectors can hinder the packaging process for miniaturization purposes and large-scale fabrication. Thus, Lissajous point scanning has been used as the method of choice for many studies [30–32]. Improvements in image reconstruction [33], tradeoffs among the frame rate, pixel resolution, and scan pattern density [34], and frequency selection rules [35] are being investigated.

Scanning mechanisms are being scaled down in size using Micro-Electro-Mechanical Systems (MEMS) technologies for use in endomicrosopes [36–38]. The miniature dimensions allow for placement of the scan mirror in the distal end of the instrument where greater control of the focus can be achieved. Parametric resonance scanning mechanisms can achieve fast scan speeds with hysteresis free behavior using low power consumption in a small footprint [39,40]. We have developed compact, monolithic 3-axis scan mirrors to achieve wide lateral deflections and large axial displacements [41–44]. The scan mode can be "switched" to image in either the horizontal or vertical plane by tuning the drive frequency in a regime that features mixed softening/stiffening dynamics. The beams can be deflected at wide angles that are limited only by the scanning mechanism rather than by the diameter of the objective lens. These scan mirrors can be batch fabricated using simple processes whereby hundreds of devices can be produced on a single silicon wafer and scaled up for mass manufacture. By comparison, conventional microscopes use bulky scan mechanisms, such as galvos, that are large in dimension and must be placed in the pre-objective position.

The dual axes configuration can be used to collect NIR fluorescence images with high spatial resolution and increased tissue penetration depth. IRDye800 can be administered intravenously to generate high contrast using excitation at $\lambda_{ex} = 785$ nm. This approach can be used for early cancer staging. This instrument can also be used for image-guided surgery to identify the boundaries between the normal and diseased tissues. Other efforts in this area include use of longer wavelength illumination [23,45], Bessel beam profiles [46,47], and different detection methods (e.g. lock in detection in Modulated-Alignment Dual-Axis (MAD) confocal microscopy [13,48]). The use of NIR excitation provides increased penetration depth in tissue, a highly scattering medium [49].

Here, we aim to scale down the diameter of a dual axes confocal endomicroscope to <4.2 mm. This reduction in dimensions allows for repetitive insertion into hollow organs of genetically engineered mice to perform longitudinal in vivo imaging. A side-view geometry allowed the focusing optics to be positioned at normal incidence to the mucosal surface [50,51]. This orientation can cover a significantly larger mucosal surface area by using an axial push-pull motion combined with angular rotation compared with a front-view design. A custom monolithic 3-axis scan mirror was designed for use in this instrument. The dimensions of the reflector were defined to match that of the illumination and collection beams over the range of angular deflections and axial displacements. Torsional and serpentine springs were designed to achieve

frame rates >5 Hz for real-time imaging. The scan mirror was placed in the post-objective location to control the focus in 3-axes, and generate images in horizontal and vertical planes. In vivo images were collected from normal and pre-malignant colonic mucosa in live genetically engineered animals using IRDye800 for systemic contrast to demonstrate deep tissue penetration over a large FOV with sub-cellular resolution.

2. Materials and methods

2.1. Imaging system

A schematic of the imaging system is shown, Fig. 1. A fiber-coupled solid-state laser (TOPTICA Photonics, #iBEAM-SMART-785-S) was used to provide NIR excitation at λ_{ex} = 785 nm (max 200 mW). The excitation beam was focused into a one meter-long single-mode fiber (SMF$_1$, NA = 0.13, Nufern, #780 HP) with a 5 ± 0.5 μm mode field diameter. The two beams were collimated using a set of custom 1.8 mm diameter fiber-pigtailed gradient index (GRIN) collimating lenses (C$_1$ and C$_2$, GrinTech GmbH, #GT-CFRL-180-025-20-NC) with a center-to-center distance of 1.9 mm. Risley prisms (RP), consisting of 2 custom 0.2° optical wedges, could be inserted in the illumination path and rotated to achieve fine alignment of the two beams in parallel. The wedges (Nanjing Shuncheng Optical Components Ltd) were 1.8 mm diameter and fabricated from N-BK7 glass with anti-reflection coating to achieve reflectivity R < 0.5% between 600-1050 nm. The objective lens L$_1$ focuses the illumination and collection beams to converge at the focal point below the tissue surface. A scan mirror (M) placed in the post-objective position deflects the two beams synchronously through the solid immersion lens (SIL) L$_2$.
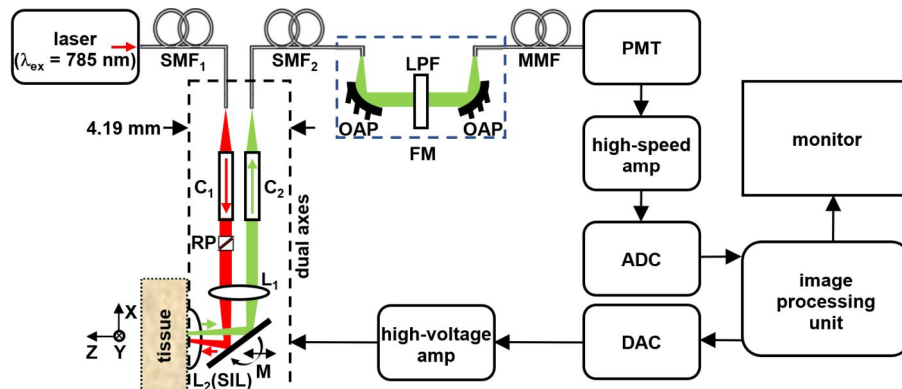

Fig. 1. Schematic. Laser excitation at λ_{ex} = 785 nm was delivered to a 4.19 mm diameter dual axes confocal endomicroscope with a side-view configuration. Details are provided in the text. Key: L – lens, SMF – single mode fiber, C – collimator, RP – Risely prism, M – scan mirror, SIL – solid immersion lens, LPF – long pass filter, OAP – off-axis parabolic mirror, MMF – multi-mode fiber, PMT – photomultiplier tube, ADC – analog/digital converter, DAC – digital/analog converter.

Fluorescence (green) was collected, descanned by M, transmitted through a second collimating lens C$_2$, and into a second single mode fiber SMF$_2$. The collection beam exits SMF$_2$, and is delivered into an inline fiber optic filter mount (FM, Thorlabs, #FOFMF) where two off-axis parabolic (OAP) mirrors collimate the fluorescence beam and provide high reflectance (>97%) between 400-2000nm with achromatic performance. An ultra-steep long pass filter (LPF, Semrock, #LP02-785RU-25) transmits between 795.2-1770.7 nm with >93% efficiency and rejects the excitation beam. Fluorescence is delivered through a multi-mode fiber (MMF, Thorlabs #M72L01) to a photomultiplier tube detector (PMT, Hamamatsu, #H7422-40). A

high-speed amplifier (Edmund Optics, #59-179) was used to convert the current signal into a voltage. A multi-function data acquisition board was used to digitize the signal from the PMT via an analog-to-digital converter (ADC, National Instruments, #PCI-6115) at 10 Msamples/sec. This board generates control signals from a digital-to-analog converter (DAC) for delivery to a high-voltage amplifier (Tegam, #2350) to drive the scan mirror. Custom software was developed to control the imaging system (National Instruments, LabVIEW). The prototype was packaged in a 4.19 mm OD tube.

2.2. Optical design

Ray trace simulations were performed using Zemax (version 22.2) in both sequential and non-sequential modes to identify commercially available optics to achieve near diffraction-limited resolution on-axis with the scan mirror in the neutral position. Objective lens L_1 (f = 5.5 mm @635 nm, NA = 0.6, Edmund Optics, #87-146) was identified to focus the two beams. An aspheric geometry was chosen to minimize spherical aberrations. The perimeter of this objective was diamond turned to reduce the diameter to 3.81 mm, resulting in an NA = 0.41. A miniature scan mirror was placed in the post-objective position to direct the two beams at a 90° angle through L_2. The lens L_2 (f = 2 mm @588 nm, Edmund Optics, #65-297) with NA = 0.5 and refractive index n = 1.83 @ 852.1 nm was used to provide contact with the tissue surface and protect against bodily fluids. L_2 was inserted with a precision sliding fit (H7/h6) into a 2 mm nominal diameter hole, and was sealed with UV-curable glue (Norland Products Inc, #NOA 61). The focused beams pass at a half angle of $\alpha = 16.2°$ through the SIL. An overall effective NA = 0.21 was determined from the ray trace simulations. All lenses fit inside an uncoated stainless steel tube (SST) with a 4.19 mm outer diameter (OD) and 3.81 mm inner diameter (ID).

With the scan mirror located at +150, 0, and -150 μm in the Z-axis, the lateral resolution calculated was 1.04, 1.02, and 0.96 μm, respectively, and the axial resolution was 6.26, 5.80, 5.08 μm, respectively. The non-sequential Zemax simulation, which includes the effect of aberrations, revealed a 1.15 and 6.9 μm resolution at Z = 0 μm. The focus moves vertically at depths between -167 μm and +143 μm (310 μm total) and laterally from -143 to +166 μm (309 μm total). The overall dimension traversed in the oblique plane is 438 μm.

The reflector dimensions were determined by the footprint generated by the incident illumination and collection beams on the scan mirror as it moves over the axial range. The two dominant configurations occur when Z is at ±150 μm, and the tilt angle around X is -8.5°. The beam dimensions on the reflector surface at the Z-axis location and tilt angles of (+150 μm, -8.5°), (0 μm, -8.5°), and (+150 μm, -8.5°) are shown by the red, green, and blue ellipses, respectively, Fig. 2(C).

2.3. MEMS scanner device

A compact, monolithic 3-axis scan mirror was designed and fabricated using MEMS processes. Two separate reflectors for the illumination and collection beams were designed with dimensions of 790×1080 μm², and were connected by struts, Fig. 3(A). The mirrors were mounted on a gimbal frame to reduce cross-talk between the X- and Y- as well as the X- and Z-axes. Electrostatic comb-drive actuators provide rotation about either the X (inner) or Y (outer) axis, respectively, and consist of comb-fingers patterned in the device layer with a 5 μm gap and are alternately movable and stationary. Symmetric through holes were introduced in the device layer to mitigate air damping during dynamic reflector motion. The through holes were located in the areas that contributed least to the expected reflector function. Including the gaps between the comb fingers, the total through-hole area accounted for ~29% of the total footprint of the moving parts (area surrounded by the backside substrate in Fig. 3(A)).

The scan mirror design was optimized to achieve >300 μm axial displacement of the focus. The gimbal suspension has 1.2 mm lever arms, defined by the distance between the outer and
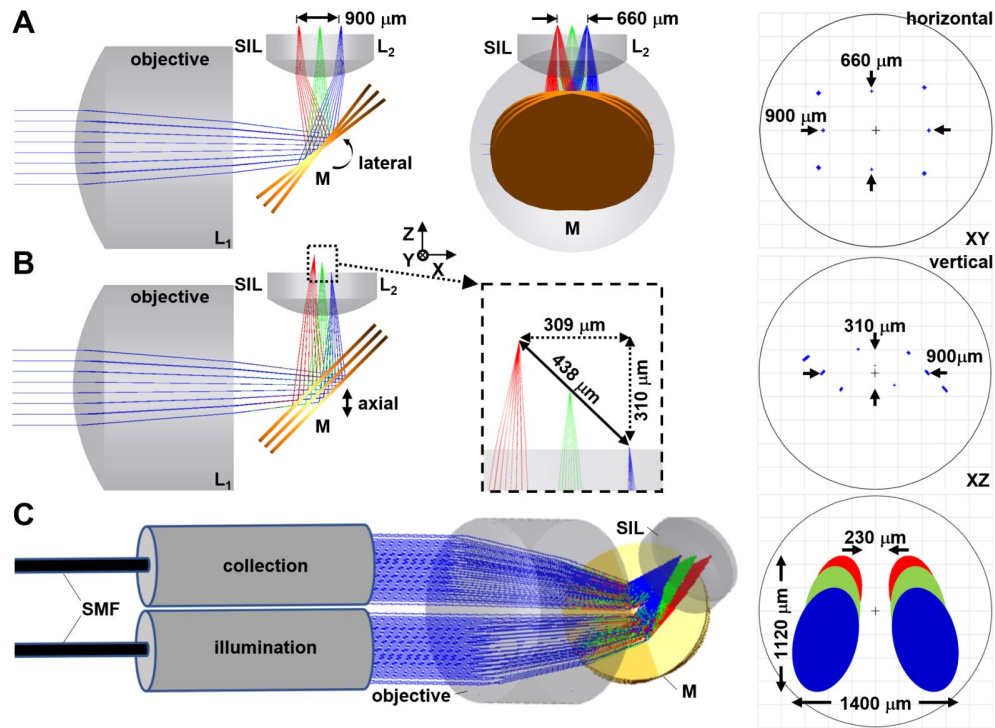
Fig. 2. Side-view geometry. A scan mirror was located in the post-objective position, and provides A) wide lateral deflections to achieve images with dimensions of 900×660 μm^2 in the horizontal plane (XY), and B) large axial displacements to produce images with dimensions of 900×310 μm^2 in the vertical plane (XZ). C) The illumination and collection beams form a pair of elliptical spots on the reflector surface. The dimensions of the area traced is shown with $\pm 8.5°$ and $\pm 9°$ lateral deflections in the X and Y-axes, respectively, and ± 150 μm in the Z-axis.
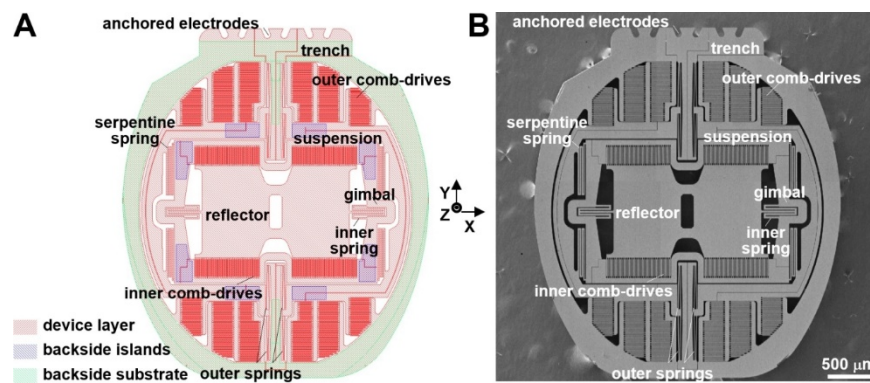

Fig. 3. Scan mirror design. A schematic is shown for the monolithic 3-axis scan mirror designed for use in the side-view dual axes prototype. A) Front side structures in the device layer (50 μm) and islands (150 μm) in the backside substrate (350 μm) were identified. B) Scanning electron micrograph (SEM) image shows a representative fabricated device with overall dimensions of 4.1×3.6 mm^2.

serpentine springs. This dimension was maximized to achieve the largest axial displacement allowed by the chip dimensions. The gimbal was attached to U-shaped suspensions via S-shaped serpentine springs located in each corner to determine the resonance frequencies for imaging in the vertical plane. The suspensions act as a lever to either rotate the mirror around the outer Y-axis or displace out-of-plane in the Z-axis to achieve unprecedented axial translation of the focal point. The outer comb-drives were arranged in 3 columns to generate a large force to produce angular deflections of $>23°$ ($\pm11.5°$) and achieve out-of-plane mirror motion $>400\,\mu m$ ($\pm200\,\mu m$).

2.3.1.   Spring design

The resonance frequency in the X-axis (inner) was determined by two torsional springs arranged symmetrically on either side of the reflector. The resonance frequency in the X-axis was chosen to achieve a frame rate >5 per sec to mitigate motion artifacts during in vivo imaging. The resonance frequency in the Y-axis (outer) was determined by four torsional springs that consisted of symmetric sets of beams oriented in a trapezoidal geometry that connected to the suspension and served as an anchor in the substrate. This configuration reduces stress on the springs to allow for greater axial displacement and to counteract the "pull-in" effect from non-linear motions generated by large electrostatic forces. Several spring design geometries were considered to provide wide angular deflections and large axial displacements. A > 5% gap was introduced between desired and undesired eigenmodes to eliminate unwanted motions. Spring designs with wide cross sections were selected to mitigate the effect of process variations and improve fabrication yield.

When the drive signal to the outer comb-drives approached a frequency near twice that of the eigenmode, the actuators rotate the suspension (and reflector) for slow scanning about the Y-axis in the horizontal plane. At a reduced drive frequency, the suspensions then act as levers to displace the mirror with large out-of-plane motion in the vertical plane (Z-axis). Thus, by tuning the drive frequency, the scanner mode can be "switched" to image in either the horizontal or vertical planes. The frequencies required to achieve optimal Lissajous scanning in the XY and XZ planes at 5 frames per sec were identified using custom MATLAB software (Mathworks).

2.3.2.   Finite element model

Scanner operation was based on the principle of parametric resonance [39]. The drive signal has a frequency near twice that of the corresponding eigenmode. Electrostatic comb-drive actuators were used to produce either wide lateral deflections or large axial displacements by tuning the frequency, voltage, and square wave duty cycle of the drive signal. The scan mirror can be "switched" instantaneously (at the cost of one frame) between horizontal and vertical modes by adjusting the drive frequency. When switching between the two imaging planes, the first frame can be affected due to the damp down of the previous resonance motion and ramp up of the new resonance motion associated with the new imaging plane. A finite element model (FEM) was developed using COMSOL software to identify the resonant frequencies to minimize interference from parasitic vibrations that can distort the image. These unwanted motions result from mechanical and capacitive coupling of either super or sub-harmonic frequencies near the drive frequency. This phenomenon is well-known in parametric resonance scanners. The natural frequency of each mode was separated from adjacent natural or harmonic frequencies by at least 5%. This guideline was based on our previous experience with parametric resonance scanners [41–44]. The non-linear response of the scanner results from a complex interaction of electrostatic softening, mechanical hardening, and structural damping.

2.3.3. Device fabrication

A 350 μm deep cavity was etched using a 3-step deep reactive-ion etch (DRIE) process on the back side of the substrate to provide space for the mirror to displace laterally with wide angular deflections and vertically with large axial displacements. The backside islands were partially released. Trenches were etched with deep and narrow dimensions in the device layer to electrically isolate the drive signals between the inner and outer comb-drives. Backside islands were etched to provide mechanical support for the gimbal.

Symmetrical openings were etched in the device layer to reduce the effects of air damping after the scan mirror was packaged and sealed in the endomicroscope. The total surface of the device, including the reflector surface, was coated with a ~100 nm layer of aluminum (Al) via a blanket evaporation process to enhance reflectivity to >87% in the NIR spectral regime (600-900 nm) [52].

2.3.4. Device characterization

The devices were tested in ambient temperature and pressure to characterize the frequency response in 3-axes. A calibrated target was used to measure the optical scan angles, and a high-speed profile inspector (Keyence, #LJ-V7020) was used to measure the out-of-plane motion. The scan mirror was driven at frequencies approximately twice that of the expected eigenmodes. The frequency response to an upsweep (low-to-high) and down sweep (high-to-low) in the drive signal was evaluated. The voltage, wavefront, and duty cycle of the drive signals were empirically adjusted to characterize the amplitude and frequency response of the scan mirror in 3-axes. These results were used to select the best set of parameters to produce a large range of lateral and axial motions with minimal parasitic vibrations.

2.4. Instrument packaging and alignment

The scan mirror was mounted on a compact MEMS holder printed using high-resolution stereolithography, Fig. 4(A)-(C). The tail was used for safe handling and precise alignment, and was snapped off after packaging was completed. The holder was fabricated from an ABS (acrylonitrile butadiene styrene) like material with adequate elongation and stiffness using a high precision 3D printer (Proto Labs, Inc, MicroFine Gray) capable of fabricating features as small as 50 μm. Copper wires (63 μm thick) were looped around anchored electrodes (50 μm thick) etched on the periphery of the scan mirror, and were connected to the drive signal and power supply, Fig. 4(D).

A custom conductive glue was applied to enhance wire conductivity, Fig. 4(E). The glue was formed by mixing 5 grams of 99.9% silver nanoparticles (200-400 nm, SkySpring Nanomaterials Inc, #0124DX) and 5 grams of 99.95% silver nanoparticles (100 nm, SkySpring Nanomaterials Inc, #0115CY) with one ounce of conductive glue (Norland Products, #NCA 130). This mixture improved conductivity and reduced mechanical strength to avoid any malfunction or sparks at the bond site. The addition of nanoparticles reduced the mechanical strength of the glue. The wires thus were secured with UV-curable glue (Norland Products, #NOA 61) applied up to the periphery of the device right before the bond pads. A tinge of the conductive glue was then applied to the bond pads to improve the wire-pad conductivity. The high viscosity of the customized conductive glue prevented cross-over that could cause electrical shorts and device failure. A tinge of the conductive glue was then applied to the bonding pad to improve wire-pad conductivity. The high viscosity of the customized conductive glue prevented cross-over that could have caused electrical shorts and device failure.

An assembly diagram for the instrument is depicted, Fig. 5. Collimators were held in parallel using a precision CNC machined brass holder (colored in yellow). The collimators and Risley prisms sit inside the two grooves machined in parallel on this holder. A beam analysis system (Ophir Photonics, BeamScan XYS) was used to grossly align the two beams in parallel with an
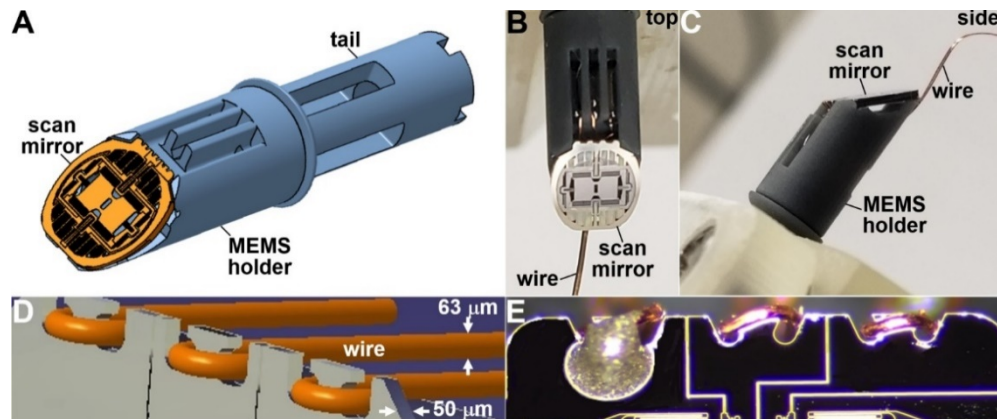
Fig. 4. Scanner packaging and wire bonding. A) The scan mirror was mounted on a MEMS holder printed using high-resolution stereolithography. The tail was snapped off after completion of packaging. B) Top and C) side views show the scan mirror mounted in the MEMS holder. D) Electrical connections were provided using 63 μm thick copper wires looped around 50 μm thick device pads on anchored electrodes and were attached to the high-voltage source. E) UV-curable conductive glue was used to enhance wire conductivity.

initial accuracy of <1 mrad. The Risley prisms were rotated over a maximum range of 1.78 mrad to achieve fine alignment. A final accuracy of <0.06 mrad between the two parallel beams was achieved. After alignment was completed, the positions of the two prisms were fixed with UV glue (Norland Products Inc, #NOA 61). Instrument assembly was performed using a carefully designed fixture containing a horizontal V-groove to secure the SST and a few 1 mm vertical through holes and grooves to achieve precise component packaging. The SST was positioned in the V-groove with the SIL facing upwards. The precise angular position around the tube axis was maintained using a 1 mm pin passed through the tube into the fixture. The SIL and objective lenses were precisely positioned inside the SST using micron precision actuators, and fixed using UV glue.

Fig. 5. Assembly diagram demonstrates key steps used to package the instrument.

Co-axial alignment of the MEMS device assembly with the SST was achieved using an H7/h6 clearance between the outer diameter of the holder and the inner diameter of the tube. The angular position was controlled using a 1 mm pin that passed through the tail into the fixture. The position along the axis was controlled using the raised ring stop at the end of the main body

of the MEMS holder. Once the collimator beams were aligned in parallel, the sub-assembly was packaged in the SST. Co-axial alignment with the SST was assured using an H7/h6 clearance between the outer diameter of the brass collimator holder and the inner diameter of the tube. The angular position was controlled using a 1 mm pin that seated in the 1 mm groove on the end and was passed in a 1 mm wide groove in the fixture. This pin also acted as a stop to control the position along the tube axis. After precise positioning, each sub-assembly was fixed in place using UV glue.

A photo is shown of the packaged endomicroscope with a 4.19 mm OD and 45 mm rigid length, Fig. 6(A). This instrument passes easily into the colon of a live mouse, Fig. 6(B). The side-view geometry allows the focusing optics to be placed in direct contact with the mucosal surface to facilitate the collection of high quality images in vivo. The outer diameter provided a dimension that could be inserted repetitively in hollow organs, such as the colon, of live animals to perform longitudinal imaging studies.
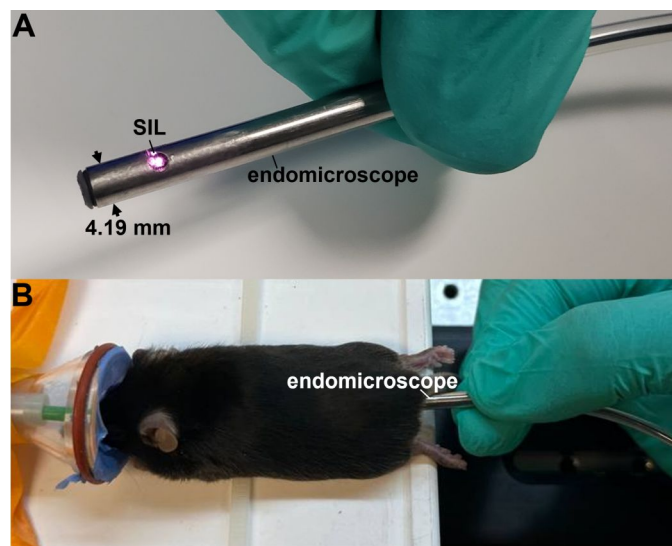

Fig. 6. Prototype instrument. A) Photo is shown of the packaged endomicroscope with a 4.19 mm outer diameter and 45 mm rigid length. B) This instrument passed seamlessly into the colon of an anesthetized live genetically-engineered mouse. With a side-view geometry, the focusing optics can be placed easily in contact with the mucosal surface.

2.5. Image resolution

The lateral resolution was measured using a knife-edge approach whereby the distance spanning 10%-90% of the maximum intensity across a step intensity border of a USAF 1951 target was determined. Results were confirmed by collecting a reflectance image from a standard (USAF 1951) resolution target. The axial resolution was measured by translating a plane mirror and passing the focal point in the vertical direction in a scatter-free air film and quantifying the full-width-at-half-maximum (FWHM).

2.6. In vivo images

All experimental procedures were performed in accordance with the relevant guidelines and regulations of the University of Michigan. Animal imaging studies were conducted with approval by the University Committee on the Use and Care of Animals (UCUCA). *CPC;Apc* mice that have been genetically engineered to sporadically delete the APC gene were used, and adenomas that

develop spontaneously in the colon were imaged [53]. The mice were housed in pathogen-free conditions and supplied water ad libitum under controlled conditions of humidity ($50 \pm 10\%$), light (12/12 hour light/dark cycle), and temperature (25 °C).

IRDye800 (LI-COR Biosciences) was administered intravenously via tail vein (300 μM, 200 μL PBS) to generate NIR fluorescence. After 20 min for the contrast agent to circulate, the instrument was inserted into the anus. A lubricating gel (EcoVue, Nissha Medical Technologies) was used to facilitate entry, if needed. The instrument was advanced into the colon. In the side-view configuration, the focusing optics was oriented at normal incidence to the mucosal surface. The SIL was maneuvered to achieve comprehensive contact of the optics with the epithelium. NIR fluorescence images of normal and pre-malignant (dysplasia) lesions were collected in vertical and horizontal planes by tuning the drive frequency to the scan mirror. Videos were captured at 5 frames per sec, and were exported in .avi format with 8-bit (grayscale) resolution. Video streams that showed minimum motion artifacts were identified. After completion of imaging, the mouse was euthanized, and the colon was resected, fixed in 10% buffered formalin, and processed for routine histology (H&E).

3.   Results

3.1.   MEMS scanner device

Finite element modal analysis of scan mirror motion was performed using COMSOL software. The first, second, and fourth eigenmode (EM) represented the Z-axis translational mode (852.2 Hz), Y-axis torsional mode (1000.4 Hz), and X-axis torsional mode (4384.2 Hz), respectively. The 350 μm deep cavity etched on the backside allowed the mirror to tilt at large angles and to displace vertically. The island structures were engaged in each axis during motion, Fig. 7(A)-(C) (side-view).
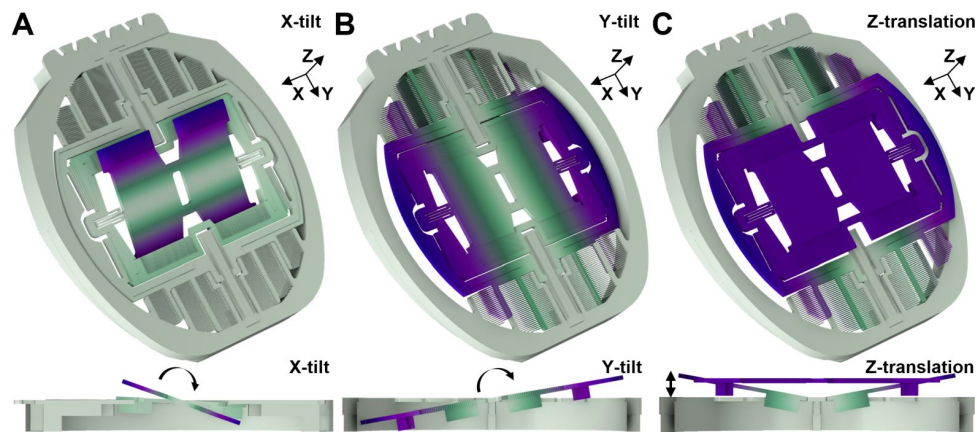

Fig. 7. 3-axis motion. CAD drawing shows areas of active motion in the monolithic 3-axis scan mirror for A) X-tilt, B) Y-tilt, and C) Z-translation. Side-view shows the motion of scanner components, including backside islands. The color map shows the total displacement magnitude (pale green to dark blue corresponds to zero to max amplitude).

Torsional and serpentine springs were designed with geometry and dimensions to achieve wide angular deflections in the inner (X) and outer (Y) axes, Fig. 8(A),(B), and large out-of-plane motion in the Z-axis, Fig. 8(C), respectively. This set of figures shows that the springs undergo severe deformations to achieve the full range of motion.

An optical scan range of nearly ±26.5° around the X-axis and ±23.5° around the Y-axis was measured on the optical bench, Fig. 9(A),(B). An out-of-plane displacement of >410 μm in the
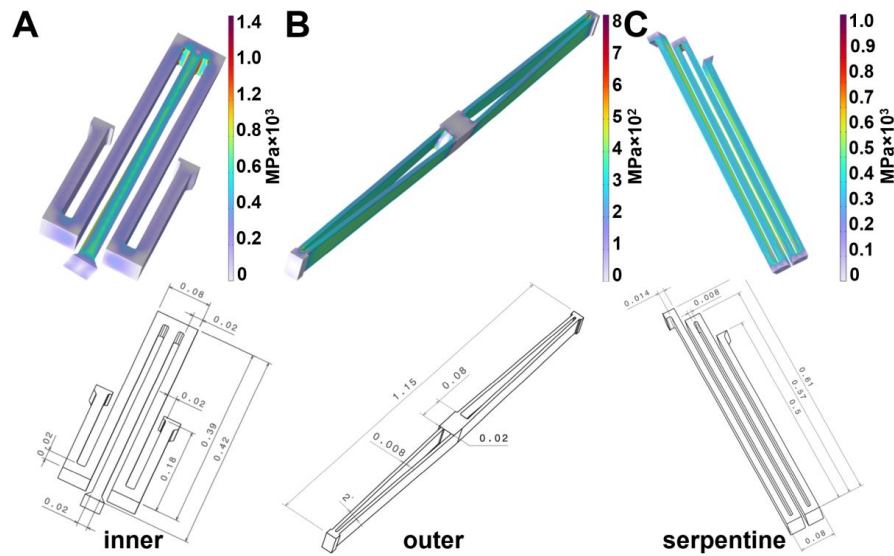
Fig. 8. Spring designs. Geometry and dimensions are shown for A) inner torsional, B) outer torsional, and C) serpentine springs. Heatmap predicts the mechanical stress present throughout the structures as simulated using a finite element model (FEM).

Z-axis was demonstrated, Fig. 9(C). The very large motions have been described by complex interactions resulting from electrostatic softening, air damping, and mechanical hardening. Images with an expected FOV of 660×900 and $900 \times 310 \ \mu m^2$ were collected in horizontal and vertical planes.

Different sets of drive signals were applied to the scanner to achieve the desired image dimensions and frame rates. A dense Lissajous scan pattern was formed at 5 frames per sec, and generated images in either the vertical or horizontal plane with dimensions of 900×310 or $900 \times 660 \ \mu m^2$, respectively, at >99.9% coverage.

3.2. Image resolution

A lateral resolution of 1.75 µm was measured from the transition width between 10% to 90% of the maximum intensity from a line profile across a knife-edge target, Fig. 10(A). An axial resolution of 7.50 µm was measured using the full-width-at-half-max (FWHM), Fig. 10(B). By comparison, the Zemax simulation predicted a lateral and axial resolution of 1.12 and 7.07 µm, respectively.

A reflectance image from a standard resolution target was collected in the horizontal plane to qualitatively estimate a lateral resolution of ∼2 µm, Fig. 10(C). Individual bars from group 7, element 6 are clearly seen (red oval). A FOV of $900 \times 660 \ \mu m^2$ in the horizontal plane was supported by a grid target consisting of $50 \times 50 \ \mu m^2$ boxes, Fig. 10(D). The full image FOV could not be captured by this planar target because post-objective scanning sweeps out a curved surface. A vertical imaging depth of 220 µm in the air was measured using a microtrench phantom etched in a zig-zag pattern, Fig. 10(E). This value corresponds to 310 µm in tissue based on Zemax simulations using n = 1.38 as the tissue refractive index. The working distances for the XY and XZ images were 170 and 0 µm, respectively. No coupling medium was used.
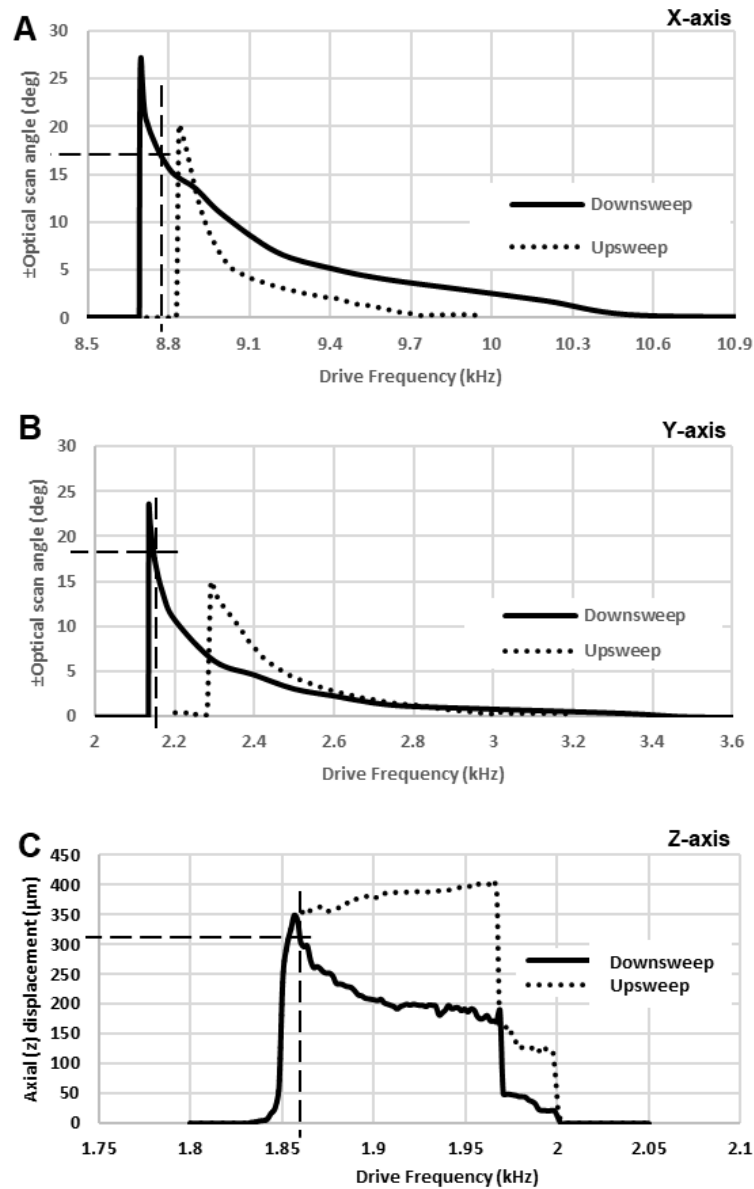
Fig. 9. Frequency response of scan mirror. Large lateral deflections in the A) inner (X) and B) outer (Y) axes are shown versus drive frequency using a square wave with 30% duty cycle and voltage of 60 V_{pp} during a frequency downsweep. C) The magnitude of the out-of-plane displacement in the Z-axis is shown versus drive frequency using a square wave with 50% duty cycle and voltage of 80 V_{pp} during a frequency downsweep and upsweep. The dashed line represents the selected set-points for actuating the scan mirror.

3.3. In vivo images

3.3.1. Vertical cross-sectional images

The endomicroscope was inserted in the colon of a live mouse. Real-time NIR fluorescence images of normal and pre-malignant (dysplasia) colonic mucosa were collected in vivo in the vertical
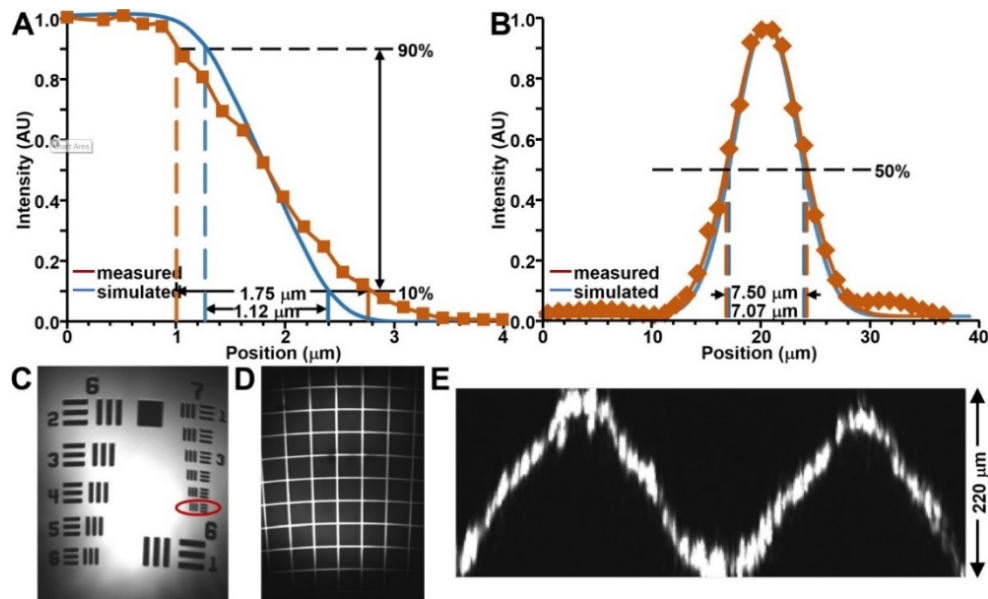
Fig. 10. Image resolution. A,B) Lateral (10-90% of peak value) and axial (FWHM) resolution of 1.75 and 7.5 μm, respectively, were measured. By comparison, the Zemax simulation predicted a lateral and axial resolution of 1.12 and 7.07 μm, respectively. C) A reflectance image collected from a standard (USAF 1951) bar target distinguishes group 7-6 (red oval). D) Image from a grid pattern (50 μm² boxes) shows a FOV of 900×660 μm². E) Image of a microtrench phantom etched in a zig-zag pattern shows a 220 μm depth in the vertical plane.
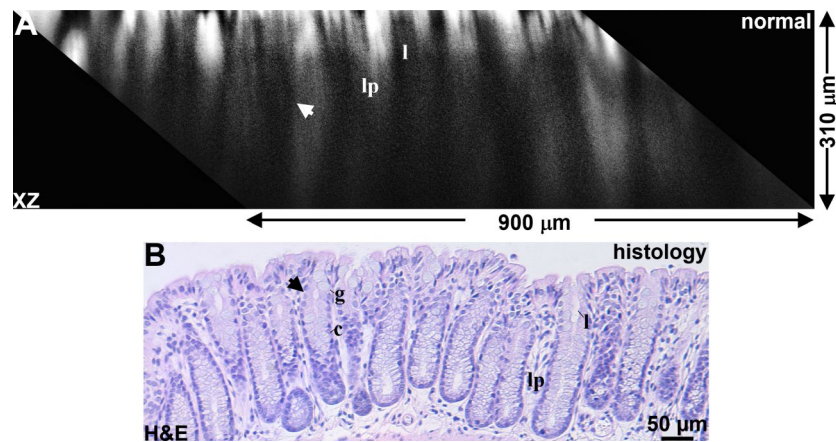

Fig. 11. Vertical cross-section of normal colonic mucosa. A) NIR fluorescence image was collected in vivo in the vertical plane over a depth of $Z = 310$ μm following intravenous injection of IRDye800 (300 μM in 200 μL PBS). See Visualization 1. B) Representative histology (H&E) in the vertical plane is shown. Mucosal details, including crypts (arrow), colonocytes (c), goblet cells (g), lumen (l), and lamina propria (lp), could be distinguished.

plane with a FOV of 900×310 μm², Fig. 11(A), and Fig. 12(A), respectively. Normal crypts appeared with relatively uniform size, even spacing, and tall columnar structures. Dysplastic crypts appeared with variable size, uneven spacing, and disorganized structures. The images
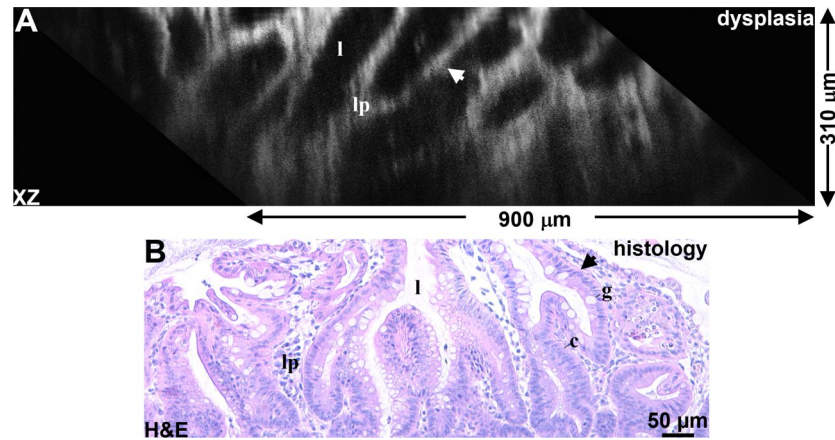
Fig. 12. Vertical cross-section of dysplasia. A) NIR fluorescence image was collected in vivo in the vertical plane for dysplasia over a depth of Z = 310 μm following intravenous injection of IRDye800 (300 μM in 200 μL PBS). See Visualization 2. B) Representative histology (H&E) in the vertical plane is shown. Mucosal details, including crypts (arrow), colonocytes (c), goblet cells (g), lumen (l), and lamina propria (lp), could be distinguished.
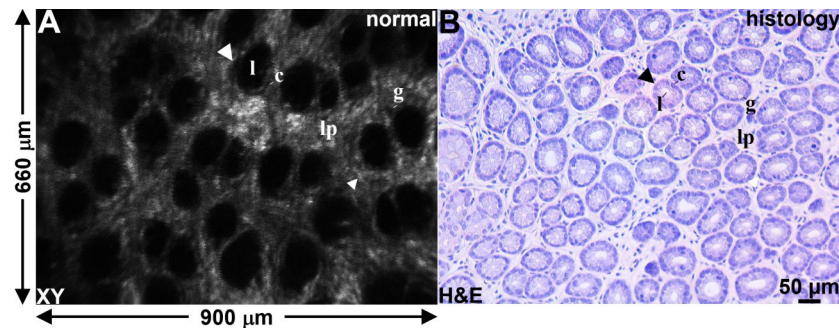

Fig. 13. Horizontal cross-section of normal colonic mucosa. A) Optical section collected in the horizontal plane of normal colonic mucosa at an axial depth of Z = 170 μm is shown following intravenous injection of IRDye800 (300 μM in 200 μL PBS). Mucosal details can be appreciated, including crypt structure (arrow) with central lumen (l) surrounded by lamina propria (lp). Individual cells can be distinguished, including colonocytes (c), goblet cells (g), and inflammatory cells (arrowhead). See Visualization 3. B) Representative histology (H&E) for normal in the horizontal plane is shown.

collected were consistent with representative histology (H&E), Fig. 11(B) and Fig. 12(B). The animals showed no signs of pain or trauma, such as inactivity and bleeding, either during or following the completion of imaging.

3.3.2. Horizontal cross-sectional images

Real-time NIR fluorescence images of normal and pre-malignant (dysplasia) colonic mucosa were collected in vivo in the horizontal plane with a FOV of 900×660 μm^2, Fig. 13 and Fig. 14, respectively.

These images were collected at a depth of Z = 170 μm, the neutral position of the scan mirror established during packaging. Normal crypts appeared circular in shape, relatively uniform in diameter, and even in spacing, Fig. 13(A). Dysplastic crypts appeared with variable size, uneven
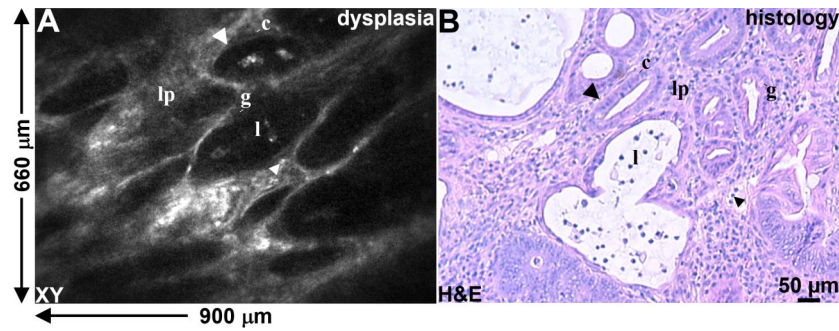
Fig. 14. Horizontal cross-section of colonic dysplasia. A) Optical section collected in the horizontal plane of dysplasia at an axial depth of Z = 170 μm following intravenous injection of IRDye800 (300 μM in 200 μL PBS). The mucosa exhibits substantially enlarged crypts (arrow), distorted lumens (l) surrounded by crowded lamina propria (lp). Individual cells can be distinguished, including colonocytes (c), goblet cells (g), and inflammatory cells (arrowhead). See Visualization 4. B) Representative histology (H&E) for dysplasia in the horizontal plane is shown.

spacing, and heterogenous shapes, Fig. 14(A). Individual cells, including colonocytes, goblet cells, and inflammatory cells, could be distinguished in the horizontal plane. Representative histology (H&E) confirmed these observations, Figs. 13(B),14(B).

4.   Discussion

Here, we demonstrate a 4.19 mm diameter side-view dual axes confocal endomicroscope. This geometry allows the focusing optics to be placed in direct contact with the mucosal surface in hollow organs to collect in vivo imaging. A compact, monolithic 3-axis scan mirror was designed and fabricated using MEMS technology to match the instrument dimensions. This compact device generated lateral deflections of ±26.5° and ±23.5° in the X and Y-axes, and axial displacements >410 μm in the Z-axis. Placement of the scan mirror in the post-objective position resulted in the formation of images with a very large FOV >900 × 660 and >900 × 310 μm^2 in horizontal and vertical planes, respectively, in tissue. This device combined the softening dynamics of electrostatic transduction with the stiffening dynamics of the lever structure to substantially extend the range of motion [41–44]. The scan mode can be "switched" between either wide angular deflections or large axial displacements by tuning the drive frequency. The focusing optics had an overall NA = 0.21 to produce a lateral and axial resolution of 1.75 and 7.5 μm, respectively. In vivo images were collected at 5 frames per sec using excitation at λ_{ex} = 785 nm following intravenous injection of IRDye800 to generate NIR fluorescence contrast. Individual cells, including colonocytes, goblet cells, and inflammatory cells, could be identified in the horizontal cross-sectional images. Also, mucosal structures, including crypts, lumens, and lamina propria, could be distinguished in either the vertical or horizontal cross-sectional images.

This reduction in diameter allowed for repetitive insertion into hollow organs of live animals. Longitudinal investigations can be performed in the epithelium of genetically engineered mice to elucidate mechanisms for normal development and the natural history of disease processes. The scan mirror produced large out-of-plane Z-axis displacement to achieve an imaging depth >300 μm, which is adequate to investigate many epithelial processes. The vertical plane provides the natural direction for disease progression and provides the same orientation as that used by pathologists to evaluate histology. Also, the scan mirror produced wide angular deflections to achieve a large FOV >900 × 660 μm^2 in the horizontal plane. These dimensions were achieved using post-objective scanning, and are much larger than that of other endomicroscopes with

similar size. The ability to track individual epithelial cells in vivo for an extended period of time (hours to days) in live animals can substantially increase our scientific understanding of fundamental biological mechanisms. This thin layer of tissue lines all hollow organs and is highly regenerative and metabolically active [54]. The thickness is only several hundred microns and is well suited for interrogation using the instrument demonstrated.

The 4.2 mm diameter side-view configuration offers a number of advantages in comparison with the previous 5.5 mm front-view instrument. Scaling down the diameter of the front-view configuration for internal use in live animals is challenging because the parabolic mirror focusing element has a thin and fragile body that increases manufacturing and packaging costs. Also, in the side-view architecture, the reflector was oriented in the tube at a 45° angle to the incident beams, and provided >59% more area to accommodate the MEMS chip (4.1×3.6 versus 3.2×2.9 mm^2). This increase in space allows for greater flexibility to design the microstructures of the scan mechanism. The additional space allowed for inclusion of more comb-drive actuators to generate a greater electrostatic force to move larger structures. The lever arms of the suspension could be lengthened to increase the axial displacement of the reflector. Although the reflector footprint was >77% larger than that in the 5.5 mm design, the reflector tilt angles, and out-of-plane motions were comparable. Larger through holes were introduced around the reflector to mitigate air-damping effects after the scanhead was sealed. A low-cost, commercially available aspheric optic rather than a parabolic reflector could be used as the focusing element. Also, the larger size of the MEMS device resulted in less complexity in the fabrication process and greater ease of device handling.

Several limitations had to be overcome to optimize the imaging performance in the side-view configuration. The reduced form factor shrinks the angle between the excitation and collection beams and reduces the axial resolution. However, the side-view architecture allowed for using collimators with 1.8 mm diameter, resulting in $\alpha = 16.2°$ to improve axial resolution. This came with the cost of reducing the internal space available for packaging and limited the choice of material with dimensional stability to align the collimators with micron precision. A CNC micro-machined brass collimator holder was selected to overcome this problem due to the ease of machining, stiff rigidity, dimensional stability, and high accuracy.

In the future, the dual axes configuration can be further improved to broaden utility. The endomicroscope can be further reduced in length and diameter to fit into the instrument channel of standard medical endoscopes and perform instant "optical" biopsy by collecting fluorescence images in the vertical plane and providing the same view as that used by pathologists. The instrument width can be reduced using smaller diameter collimators. Also, the length can be shortened by reducing the hollow region in the holder behind the MEMS chip. Collimators with shorter length can be custom-designed using plano-convex lenses rather than using the much longer GRIN collimator assemblies. The endomicroscope can be adapted for multiplexed detection by collecting visible fluorescence images in multiple channels concurrently. Laser excitation at multiple wavelengths can be delivered into the illumination fiber, and a wavelength division multiplexer can be used to separate the fluorescence bands from the collection fiber. 3D volumetric images can be generated by combining a longitudinal push/pull of the instrument with circumferential rotation. This capability would allow for monitoring of interactions among different cell populations in the tissue microenvironment over time.

By scaling down the instrument dimensions, the potential of the dual axes configuration to perform repetitive in vivo imaging in live mice has been demonstrated. Traditional methods used in biological research require the processing of resected tissues and are limited to the analysis of static events. Because animals must be euthanized to extract tissue specimens for evaluation, the time course for observing important dynamic events is prematurely shortened. The 4.19 mm diameter prototype was used to collect in vivo fluorescence images in vertical planes with a depth of 310 μm. This extent of tissue penetration is adequate to investigate the epithelium of

hollow organs, such as colon. The depth of invasion into the epithelium by cancerous lesions can be assessed to perform early cancer staging. Also, the boundary between normal and diseased regions can identified for image-guided surgery.

Finally, basic disease mechanisms can be unraveled using mice that have been genetically engineered to express optical reporters, such as barrier function, absorption, transport, microbiome, inflammation, cell signaling, metabolism, and stem cell behavior. The instrument demonstrated can help achieve a greater understanding of these fundamental processes to advance new methods for early disease detection and to identify novel targets for therapeutic intervention. This dual axes confocal endomicroscope is one of the very few miniaturized imaging systems that have the capability of real-time in-vivo imaging in horizontal and vertical planes and has superior imaging depth and axial resolution among instruments of similar or smaller diameter with such capability. It is a promising tool for monitoring human disease models in small animals and for broad scientific investigation of biomedical questions in normal development and the natural history of epithelial processes.

Disclosures. AS, KRO, and TDW are inventors on a patent filed by the University of Michigan. All other authors have nothing to declare.

Data availability. The data that support the findings of this study are available from the corresponding author upon request.

References

1. N.D. Pilonis, W. Januszewicz, and M. di Pietro, "Confocal laser endomicroscopy in gastro-intestinal endoscopy: technical aspects and clinical applications," Translational Gastroenterology and Hepatology **7**, 1 (2022).
2. K. Vyas, M. Hughes, B.G. Rosa, and G.-Z. Yang, "Fiber bundle shifting endomicroscopy for high-resolution imaging," Biomed. Opt. Express **9**(10), 4649–4664 (2018).
3. Y. Qu, P. Hu, J. Shi, K. Maslov, P. Zhao, C. Li, J. Ma, A. Garcia-Uribe, K. Meyers, and E. Diveley, "In vivo characterization of connective tissue remodeling using infrared photoacoustic spectra," J. Biomed. Opt. **23**(12), 121621 (2018).
4. G. Matz, B. Messerschmidt, W. Göbel, S. Filser, C.S. Betz, M. Kirsch, O. Uckermann, M. Kunze, S. Flämig, and A. Ehrhardt, "Chip-on-the-tip compact flexible endoscopic epifluorescence video-microscope for in-vivo imaging in medicine and biomedical research," Biomed. Opt. Express **8**(7), 3329–3342 (2017).
5. T.D Wang, "Confocal microscopy from the bench to the bedside," Gastrointestinal endoscopy **62**(5), 696–697 (2005).
6. M. Giampetraglia and B. Weigelin, "Recent advances in intravital microscopy for preclinical research," Curr. Opin. Chem. Biol. **63**, 200–208 (2021).
7. Y.W. Choo, J. Jeong, and K. Jung, "Recent advances in intravital microscopy for investigation of dynamic cellular behavior in vivo," BMB Rep. **53**(7), 357–366 (2020).
8. M.J. Pittet, C.S. Garris, S.P. Arlauckas, and R. Weissleder, "Recording the wild lives of immune cells," Science immunology **3**(27), eaaq0491 (2018).
9. G. Jacquemin, M. Benavente-Diaz, S. Djaber, A. Bore, V. Dangles-Marie, D. Surdez, S. Tajbakhsh, S. Fre, and B. Lloyd-Lewis, "Longitudinal high-resolution imaging through a flexible intravital imaging window," Sci. Adv. **7**(25), eabg7663 (2021).
10. P. Inwon and K. Pilhan, "Stabilized longitudinal In Vivo cellular-level visualization of the pancreas in a murine model with a pancreatic intravital imaging window," J. Visualized Exp. **6**(171), e6528 (2021).
11. M. Turk, V. Naumenko, D.J. Mahoney, and C.N. Jenne, "Tracking cell recruitment and behavior within the tumor microenvironment using advanced intravital imaging approaches," Cells **7**(7), 69 (2018).
12. T.D. Wang, M.J. Mandella, C.H. Contag, and G.S. Kino, "Dual-axis confocal microscope for high-resolution in vivo imaging," Opt. Lett. **28**(6), 414–416 (2003).
13. T.D. Wang, C.H. Contag, M.J. Mandella, N. Chan, and G.S. Kino, "Dual-axes confocal microscopy with post-objective scanning and low-coherence heterodyne detection," Opt. Lett. **28**(20), 1915–1917 (2003).
14. T.D. Wang, C.H. Contag, M.J. Mandella, N.Y. Chan, and G.S. Kino, "Confocal fluorescence microscope with dual-axis architecture and biaxial postobjective scanning," J. Biomed. Opt. **9**(4), 735–742 (2004).
15. L. Wei, C. Yin, and J.T. Liu, "Dual-axis confocal microscopy for point-of-care pathology," IEEE J. Sel. Top. Quantum Electron. **25**(1), 1–10 (2018).

16. G. Li, H. Li, X. Duan, Q. Zhou, J. Zhou, K.R. Oldham, and T.D. Wang, "Visualizing Epithelial Expression in Vertical and Horizontal Planes With Dual Axes Confocal Endomicroscope Using Compact Distal Scanner," IEEE Trans. Med. Imaging **36**(7), 1482–1490 (2017).

17. C. Glazowski, G. Peterson, and M. Rajadhyaksha, "Compact divided-pupil line-scanning confocal microscope for investigation of human tissues," *SPIE BiOS.* Vol. 8565, (SPIE: 2013).

18. N. Iftimia, R.D. Ferguson, M. Mujat, A.H. Patel, E.Z. Zhang, W. Fox, and M. Rajadhyaksha, "Combined reflectance confocal microscopy/optical coherence tomography imaging for skin burn assessment," Biomed. Opt. Express **4**(5), 680–695 (2013).

19. J.T.C. Liu, M.J. Mandella, N.O. Loewke, H. Haeberle, H. Ra, W. Piyawattanametha, O. Solgaard, G.S. Kino, and C.H. Contag, "Micromirror-scanned dual-axis confocal microscope utilizing a gradient-index relay lens for image guidance during brain surgery," J. Biomed. Opt. **15**(2), 026029 (2010).

20. C. Yin, A.K. Glaser, S.Y. Leigh, Y. Chen, L. Wei, P.C.S. Pillai, M.C. Rosenberg, S. Abeytunge, G. Peterson, C. Glazowski, N. Sanai, M.J. Mandella, M. Rajadhyaksha, and J.T.C. Liu, "Miniature in vivo MEMS-based line-scanned dual-axis confocal microscope for point-of-care pathology," Biomed. Opt. Express **7**(2), 251–263 (2016).

21. L.K. Wong, M.J. Mandella, G.S. Kino, and T.D. Wang, "Improved rejection of multiply scattered photons in confocal microscopy using dual-axes architecture," Opt. Lett. **32**(12), 1674–1676 (2007).

22. G. Sgourakis, I. Gockel, and H. Lang, "Endoscopic and surgical resection of T1a/T1b esophageal neoplasms: a systematic review," World Journal of Gastroenterology: WJG **19**(9), 1424 (2013).

23. Z. Gao, G. Li, X. Li, J. Zhou, X. Duan, J. Chen, B.P. Joshi, R. Kuick, B. Khoury, and D.G. Thomas, "In vivo near-infrared imaging of ErbB2 expressing breast tumors with dual-axes confocal endomicroscopy using a targeted peptide," Sci. Rep. **7**(1), 14404 (2017).

24. Y. Chen, D. Wang, A. Khan, Y. Wang, S. Borwege, N. Sanai, and J.T.C. Liu, "Video-rate in vivo fluorescence imaging with a line-scanned dual-axis confocal microscope," J. Biomed. Opt. **20**(10), 106011 (2015).

25. D. Wang, Y. Chen, Y. Wang, and J.T.C. Liu, "Comparison of line-scanned and point-scanned dual-axis confocal microscope performance," Opt. Lett. **38**(24), 5280–5283 (2013).

26. L. Wei, Y. Chen, C. Yin, S. Borwege, N. Sanai, and J.T.C. Liu, "Optical-sectioning microscopy of protoporphyrin IX fluorescence in human gliomas: standardization and quantitative comparison with histology," J. Biomed. Opt. **22**(04), 46005 (2017).

27. L. Wei, C. Yin, Y. Fujita, N. Sanai, and J.T.C. Liu, "Handheld line-scanned dual-axis confocal microscope with pistoned MEMS actuation for flat-field fluorescence imaging," Opt. Lett. **44**(3), 671–674 (2019).

28. D. Wang, D. Meza, Y. Wang, L. Gao, and J.T.C. Liu, "Sheet-scanned dual-axis confocal microscopy using Richardson–Lucy deconvolution," Opt. Lett. **39**(18), 5431–5434 (2014).

29. A.K. Glaser, Y. Wang, and J.T.C. Liu, "Assessing the imaging performance of light sheet microscopies in highly scattering tissues," Biomed. Opt. Express **7**(2), 454–466 (2016).

30. H. Kim, Y.-H. Seo, J. Jeon, and K.-H. Jeong, "Lissajous scanning structured illumination microscopy," Biomed. Opt. Express **11**(10), 5575–5585 (2020).

31. L. Zhou, X. Zhang, and H. Xie, "An electrothermal Cu/W bimorph tip-tilt-piston MEMS mirror with high reliability," Micromachines **10**(5), 323 (2019).

32. P. Tinning, M. Donnachie, J. Christopher, D. Uttamchandani, and R. Bauer, "Miniaturized structured illumination microscopy using two 3-axis MEMS micromirrors," Biomed. Opt. Express **13**(12), 6443–6456 (2022).

33. C.L. Hoy, N.J. Durr, and A. Ben-Yakar, "Fast-updating and nonrepeating Lissajous image reconstruction method for capturing increased dynamic information," Appl. Opt. **50**(16), 2376–2382 (2011).

34. G. Li, X. Duan, M. Lee, M. Birla, J. Chen, K.R. Oldham, T.D. Wang, and H. Li, "Ultra-compact microsystems-based confocal endomicroscope," IEEE Trans. Med. Imaging **39**(7), 2406–2414 (2020).

35. K. Hwang, Y.-H. Seo, J. Ahn, P. Kim, and K.-H. Jeong, "Frequency selection rule for high definition and high frame rate Lissajous scanning," Sci. Rep. **7**(1), 1–8 (2017).

36. M. Kaur, P.M. Lane, and C. Menon, "Endoscopic optical imaging technologies and devices for medical purposes: state of the art," Appl. Sci. **10**(19), 6865 (2020).

37. Z. Qiu and W. Piyawattanametha, "MEMS actuators for optical microendoscopy," Micromachines **10**(2), 85 (2019).

38. L.Y. Lin and E.G. Keeler, "Progress of MEMS scanning micromirrors for optical bio-imaging," Micromachines **6**(11), 1675–1689 (2015).

39. K.L. Turner, S.A. Miller, P.G. Hartwell, N.C. MacDonald, S.H. Strogatz, and S.G. Adams, "Five parametric resonances in a microelectromechanical system," Nature **396**(6707), 149–152 (1998).

40. J. Jeon, H. Kim, H. Jang, K. Hwang, K. Kim, Y.-G. Park, and K.-H. Jeong, "Handheld laser scanning microscope catheter for real-time and in vivo confocal microscopy using a high definition high frame rate Lissajous MEMS mirror," Biomed. Opt. Express **13**(3), 1497–1505 (2022).

41. H. Li, X. Duan, Z. Qiu, Q. Zhou, K. Kurabayashi, K.R. Oldham, and T.D. Wang, "Integrated monolithic 3D MEMS scanner for switchable real time vertical/horizontal cross-sectional imaging," Opt. Express **24**(3), 2145–2155 (2016).

42. H. Li, P. Barnes, E. Harding, X. Duan, T.D. Wang, and K.R. Oldham, "Large-displacement vertical electrostatic microactuator dynamics using duty-cycled softening/stiffening parametric resonance," J. Microelectromech. Syst. **28**(3), 351–361 (2019).

43. H. Li, K.R. Oldham, and T.D. Wang, "3 degree-of-freedom resonant scanner with full-circumferential range and large out-of-plane displacement," Opt. Express **27**(11), 16296–16307 (2019).

44. W. Shahid, Z. Qiu, X. Duan, H. Li, T.D. Wang, and K.R. Oldham, "Modeling and simulation of a parametrically resonant micromirror with duty-cycled excitation," J. Microelectromech. Syst. **23**(6), 1440–1453 (2014).

45. J.T. Liu, M.J. Mandella, H. Ra, L.K. Wong, O. Solgaard, G.S. Kino, W. Piyawattanametha, C.H. Contag, and T.D. Wang, "Miniature near-infrared dual-axes confocal microscope utilizing a two-dimensional microelectromechanical systems scanner," Opt. Lett. **32**(3), 256–258 (2007).

46. Y. Chen, A. Glaser, and J.T.C. Liu, "Bessel-beam illumination in dual-axis confocal microscopy mitigates resolution degradation caused by refractive heterogeneities," J. Biophotonics **10**(1), 68–74 (2017).

47. Y. Chen and J.T.C. Liu, "Characterizing the beam steering and distortion of Gaussian and Bessel beams focused in tissues with microscopic heterogeneities," Biomed. Opt. Express **6**(4), 1318–1330 (2015).

48. S.Y. Leigh, Y. Chen, and J.T.C. Liu, "Modulated-Alignment Dual-Axis (MAD) Confocal Microscopy Optimized for Speed and Contrast," IEEE Trans. Biomed. Eng. **63**(10), 2119–2124 (2016).

49. X. Dang, N.M. Bardhan, J. Qi, L. Gu, N.A. Eze, C.-W. Lin, S. Kataria, P.T. Hammond, and A.M. Belcher, "Deep-tissue optical imaging of near cellular-sized features," Sci. Rep. **9**(1), 3873 (2019).

50. X. Duan, H. Li, F. Wang, X. Li, K.R. Oldham, and T.D. Wang, "Three-dimensional side-view endomicroscope for tracking individual cells in vivo," Biomed. Opt. Express **8**(12), 5533–5545 (2017).

51. X. Duan, H. Li, J. Zhou, Q. Zhou, K.R. Oldham, and T.D. Wang, "Visualizing epithelial expression of EGFR in vivo with distal scanning side-viewing confocal endomicroscope," Sci. Rep. **6**(1), 37315 (2016).

52. A.D Rakić, "Algorithm for the determination of intrinsic optical constants of metal films: application to aluminum," Appl. Opt. **34**(22), 4755–4767 (1995).

53. T. Hinoi, A. Akyol, B.K. Theisen, D.O. Ferguson, J.K. Greenson, B.O. Williams, K.R. Cho, and E.R. Fearon, "Mouse model of colonic adenoma-carcinoma progression based on somatic Apc inactivation," Cancer Res. **67**(20), 9721–9730 (2007).

54. H Clevers, "The intestinal crypt, a prototype stem cell compartment," Cell **154**(2), 274–284 (2013).